

Article

Effects of Nano-CeO₂ with Different Nanocrystal Morphologies on Cytotoxicity in HepG2 Cells

Lili Wang ^{1,2,†}, Wenchao Ai ^{1,†}, Yanwu Zhai ², Haishan Li ¹, Kebin Zhou ^{2,*} and Huiming Chen ^{1,*}

¹ Chinese Academy of Inspection and Quarantine, Beijing 100123, China;

E-Mails: llwang115@163.com (L.W.); aiwenchao126@163.com (W.A.); lihs@aqsiqch.ac.cn (H.L.)

² Graduate University of Chinese Academy of Science, Beijing 100049, China;

E-Mail: yyf2009319@foxmail.com

† These authors contributed equally to this work.

* Authors to whom correspondence should be addressed; E-Mails: chenhm01@163.com (H.C.); kebinzh@163.com (K.Z.); Tel./Fax: +86-10-8539-4911 (H.C.); +86-10-5389-7806 (K.Z.).

Academic Editor: Paul B. Tchounwou

Received: 30 June 2015 / Accepted: 20 August 2015 / Published: 2 September 2015

Abstract: Cerium oxide nanoparticles (nano-CeO₂) have been reported to cause damage and apoptosis in human primary hepatocytes. Here, we compared the toxicity of three types of nano-CeO₂ with different nanocrystal morphologies (cube-, octahedron-, and rod-like crystals) in human hepatocellular carcinoma cells (HepG2). The cells were treated with the nano-CeO₂ at various concentrations (6.25, 12.5, 25, 50, 100 µg/mL). The crystal structure, size and morphology of nano-CeO₂ were investigated by X-ray diffractometry and transmission electron microscopy. The specific surface area was detected using the Brunauer, Emmet and Teller method. The cellular morphological and internal structure were observed by microscopy; apoptotic alterations were measured using flow cytometry; nuclear DNA, mitochondrial membrane potential (MMP), reactive oxygen species (ROS) and glutathione (GSH) in HepG2 cells were measured using high content screening technology. The scavenging ability of hydroxyl free radicals and the redox properties of the nano-CeO₂ were measured by square-wave voltammetry and temperature-programmed-reduction methods. All three types of nano-CeO₂ entered the HepG2 cells, localized in the lysosome and cytoplasm, altered cellular shape, and caused cytotoxicity. The nano-CeO₂ with smaller specific surface areas induced more apoptosis, caused an increase in MMP,

ROS and GSH, and lowered the cell's ability to scavenge hydroxyl free radicals and antioxidants. In this work, our data demonstrated that compared with cube-like and octahedron-like nano-CeO₂, the rod-like nano-CeO₂ has lowest toxicity to HepG2 cells owing to its larger specific surface areas.

Keywords: nano-CeO₂; cytotoxicity; apoptosis; MMP; ROS; GSH; antioxidant

1. Introduction

Cerium oxide nanoparticles (nano-CeO₂) have a wide range of applications because of their desirable physical and chemical properties. They have been used extensively in catalysis, polishing glass, solid oxide fuel cells and many other applications [1,2]. It is precisely because of this extensive use in manufacturing industries, that concerns about the potential toxic effects of nano-CeO₂ in humans and its impact on the environment have increased. Recently, nano-CeO₂ has attracted considerable attention in the biomedical field. It can enter the general circulation system through the respiratory mucosal barrier, the gastrointestinal mucosal barrier and the skin barrier, after which it has access to all tissues and organs via the blood [3,4]. Many reports have demonstrated that nano-CeO₂ is cytotoxic to various tissues and cell lines [5–9]. However, other researchers have postulated that nano-CeO₂ is an antioxidant because it eliminates reactive oxygen species [10–13]. These two conflicting views are apparent on the safety of nano-CeO₂. Size, morphology and concentration of nanoparticles are known to have significant effects on their biological responses [14–16], so the different biological effects of nano-CeO₂ in these researches may be related to the size, morphology and/or concentration of the nanoparticles. Here, we aimed to compare the biological effects and toxicity of nano-CeO₂ with different nanocrystal morphologies (cube-, octahedron-, and rod-like crystals) with an aim to find the safer morphology.

Human HepG2 cells are commonly used as *in vitro* models to elucidate the pathophysiology of hepatocytes, the mechanism of cytotoxicity and in drug detection [17]. In the present study, we employed the HepG2 cell line to analyze changes in the morphology, viability, apoptosis, nuclear DNA, mitochondrial membrane potential (MMP), reactive oxygen species (ROS) and glutathione (GSH) of these cells in response to treatment with the three different nanocrystal morphologies of nano-CeO₂.

2. Materials and Methods

2.1. Synthesis and Characterization of Nano-CeO₂

Nano-CeO₂ was synthesized by hydrothermal synthesis as described previously [14,18], to give cube-, octahedron-, or rod-like crystals. The phase analysis of the ceria nanoparticles was obtained by X-ray diffractometry (XRD, MSAL-XD2, Bragg Tech. Co., Ltd, Beijing, China) using Cu K α radiation. The size and morphologies of nano-CeO₂ were characterized by transmission electron microscopy (TEM, Philips CM30, Eindhoven, The Netherlands). The specific surface area of the nano-CeO₂ was measured by Brunauer-Emmett-Teller (BET) area measurement [19].

2.2. Cell Culture

Human hepatocellular carcinoma HepG2 cells (catalog number pSC1046, purchased from the Beijing Institute of Genomics, Beijing, China) were maintained in Dulbecco's modified Eagle's medium (DMEM) containing 10% (v/v) fetal bovine serum (Hyclone, Logan, UT, USA), 100 µg/mL streptomycin (Sigma-Aldrich St. Louis, MO, USA) and 1000 IU/mL penicillin (Sigma-Aldrich). In all experiments, cells were incubated in a humid atmosphere at 37 °C with 5% (v/v) CO₂.

2.3. Cellular Morphological and Internal Structure Observation

Exponentially growing HepG2 cells (1.0×10^5 per well) were seeded into 6-well culture plates and incubated with various concentrations of nano-CeO₂ (6.25, 12.5, 25, 50, 100 µg/mL) for 24 h. Changes in gross cellular morphology after each treatment were observed using a phase-contrast inverted biological microscope (IX71/IX2, Olympus, Tokyo, Japan). After that, the cells from each sample were harvested and washed with phosphate-buffered saline (PBS). After resuspension, the HepG2 cells were fixed in 3% malondialdehyde fluid. The samples were prepared for transmission electron microscopy (TEM) and the internal structure changes of cells were observed by TEM (JEOL JEM-1200EX, JEOL Ltd., Tokyo, Japan).

2.4. Apoptosis Assay

The HepG2 cells were treated with 6.25, 12.5, 25, 50, 100 µg/mL nano-CeO₂ for 24 h. A total of 1.0×10^6 cells from each treatment was collected using trypsin (without ethylenediaminetetraacetic acid (EDTA)), centrifuged (1000×g for 5 min), and washed twice with ice-cold PBS. Cells were then stained with fluorescein isothiocyanate (FITC)-labeled annexin V and propidium iodide (PI) according to the manufacturer's instructions (Invitrogen, Carlsbad, CA, USA) and subjected to flow cytometric analysis (Beckman Coulter, Fullerton, CA, USA).

2.5. Measurement of Cell Count, and MMP, ROS and GSH Levels

A multiparametric cytotoxicity assay was performed using a cellomics high content screening (HCS) reagent HitKit as per the manufacturer's instructions (Thermo Fisher Scientific Inc., Waltham, MA, USA). This kit measures cell count, MMP, ROS and GSH.

The HepG2 cells were placed on 96 well plates in the DMEM. On the second day, the cells were treated overnight with the 6.25, 12.5, 25, 50, 100 µg/mL nano-CeO₂ and vehicle (0.1 % DMSO), respectively. After 24 h of incubation (37 °C, 5%CO₂, 100% humidity), the media were removed and the cells were stained by fluorescent probes in the same culturing medium. The fluorescent probes were: Hoechst 33342 for cell count, tetramethylrhodamine methyl ester (TMRE) for mitochondrial membrane potential, 2',7'-dichlorofluorescein (DCFH-DA) for ROS, and finally monochlorobimane (mBCL) for glutathione. Automated live-cell multispectral image acquisition was performed on a High Content Analysis (HCA) Reader (ArrayScan XTI, Thermo Fisher Scientific Inc.). The fluorescence images were captured according to the excitation and emission wavelengths of each probe: (1) 350 and 461 nm for Hoechst 33342 on channel 1; (2) 584 and 606 nm for TMRE on channel 4; (3) 504 and 529 nm for

DCFH-DA on channel 3; (4) 380 and 461 nm for mBCL on channel 2. Image analysis was performed using HCS Studio™ 2.0 software (Thermo Fisher Scientific Inc.)

2.6. Antioxidant Activity Detection

Square-wave voltammetry (SWV) was performed to examine the ability of nano-CeO₂ to eliminate the hydroxyl radical (\cdot OH) as described by Xue using a CHI 440 electrochemical workstation (CH Instruments, Inc., Austin, TX, USA) [20]. The CO-Temperature Programmed Reduction (CO-TPR) (Micromeritics Autochem II 2920, Micromeritics, Norcross, GA, USA) was carried out to measure the oxidation-reduction properties of the nano-CeO₂ using 10% CO/N₂ at a flow rate of 25 mL/min and the furnace temperature up to 900 °C at a linear ramp of 15 °C/min. The samples were pretreated at 300 °C for 1 h before analysis.

2.7. Statistical Analyses

All data are presented as the mean \pm the standard deviation (SD). Analysis of variance was used to compare values among all groups. Statistical analysis was undertaken with SPSS 10.0 (SPSS, Inc., Chicago, IL, USA) and $p < 0.05$ was considered as statistically significant ($n = 3$).

3. Results and Discussion

3.1. Characterization of the Nano-CeO₂

The nanoparticles were synthesized hydrothermally, and their XRD patterns, shown in Figure 1, indicate that these particles were composed of cerium oxide in the typical fluorite cubic structure (JCPDS 34-0394). The size and morphology of all nano-CeO₂ are shown in Figure 2, and the results are in accordance with Table 1. Based on the BET results (Figure 2 and Table 2), the particle specific surface area decreases as the particle diameter increases.

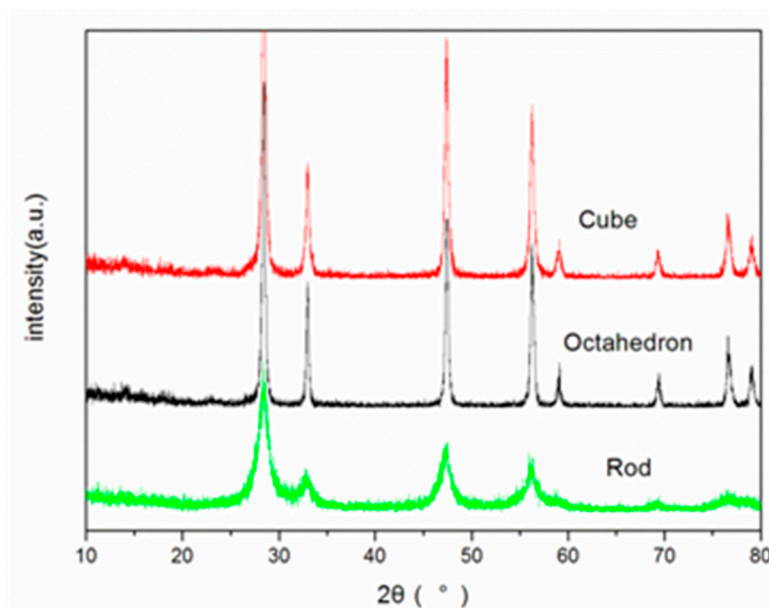


Figure 1. The XRD patterns of nano-CeO₂ synthesized by hydrothermal processing.

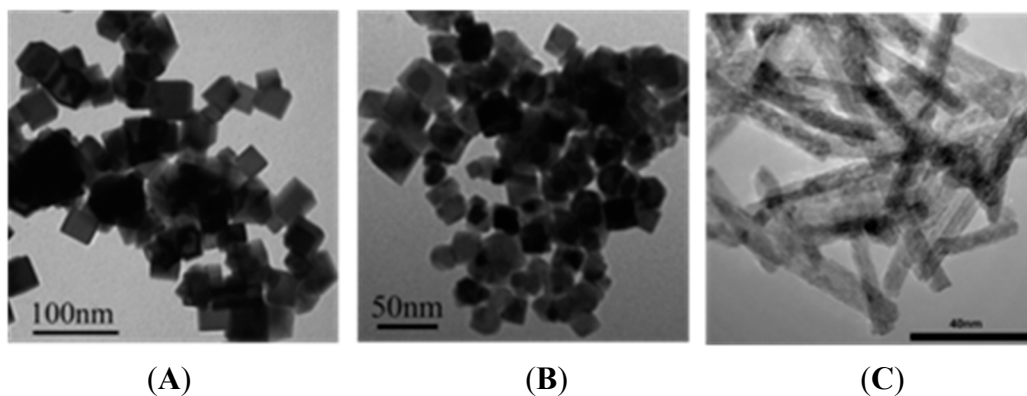


Figure 2. The TEM images of nano-CeO₂ synthesized by hydrothermal processing. (A) Cubes; (B) octahedrons; (C) rods.

Table 1. Three kinds of nano-CeO₂ with different morphologies and sizes.

| Number of nano-CeO ₂ | Morphology | Size |
|---------------------------------|------------|---|
| 1 | Cube | 20-50 nm in diameter |
| 2 | Octahedron | 10-30 nm in diameter |
| 3 | Rod | 8 nm in diameter and 100-400 nm in length |

Table 2. Surface area of synthesized nano-CeO₂.

| Number of nano-CeO ₂ | Morphology | The Specific Surface Area |
|---------------------------------|------------|--------------------------------------|
| 1 | Cube | 18.9 m ² ·g ⁻¹ |
| 2 | Octahedron | 29.9 m ² ·g ⁻¹ |
| 3 | Rod | 83.2 m ² ·g ⁻¹ |

3.2. Morphological and Internal Structure Changes of Cultured HepG2 Cells Induced by Nano-CeO₂

HepG2 cells were cultured in a full medium with one of the three types of nano-CeO₂ at 6.25, 12.5, 25, 50, 100 µg/mL for 24 h. At the end of the culture, the cells with 100 µg/mL each type of nano-CeO₂ were already damaged, while those cells cultured with 6.25, 12.5, and 25 µg/mL nano-CeO₂ showed no significant changes in morphology when compared with the control group. For the 50 µg/mL treat group, there were marked differences in the morphology of the cells between each type of nanoparticle (Figure 3). The cell junctions were disrupted, cells shapes were altered, and a large number of dead cells were present in the culture supernatant.

From these experiments, the dose (50 µg/mL) of treatment with nano-CeO₂ was chosen for subsequent TEM examination (Figure 4). All three types of nano-CeO₂ had aggregated and become localized in the lysosome and cytoplasm, accompanied by the disappearance of some lysosomal membranes. We believe the nano-CeO₂ was internalized through the endocytosis pathway, but the exact mechanism is not clear and further research is needed.

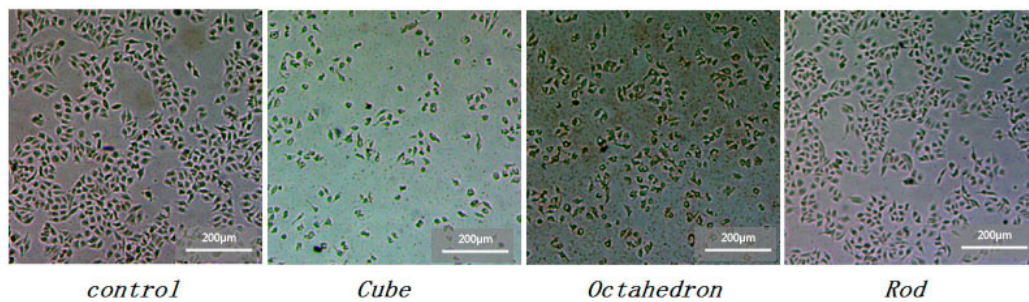


Figure 3. Photomicrographs of HepG2 cells with 50 µg/mL nano-CeO₂ demonstrating significant changes in cellular morphology.

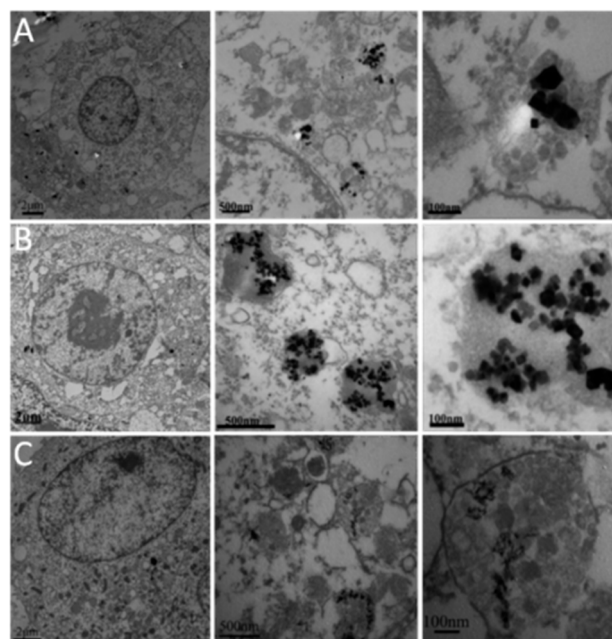


Figure 4. TEM images of HepG2 cells treated with 50 µg/mL nano-CeO₂ for 24h. (A) Cubes; (B) octahedrons, (C) rods.

3.3. Nano-CeO₂ Induced Apoptosis in HepG2 Cells

To investigate whether the observed cytotoxicity was due to apoptosis, the HepG2 cells were stained with annexin V conjugated to fluorescein isothiocyanate, which only binds to apoptotic cells. PI can penetrate into necrotic or late apoptotic cells, but does not label viable or early apoptotic cells. Meanwhile, annexin V, a protein with a high affinity for phosphatidylserine, binds to exposed phospholipids in apoptotic cells. In this study, those cells cultured with 6.25, and 12.5 µg/mL nano-CeO₂ showed no significant changes in apoptosis compared with the control group. As shown in Figure 5, increased apoptotic rates were detected in 25, 50, and 100 µg/mL nano-CeO₂-treated cells, and the increase was dose-dependent. The apoptosis percentage in the samples incubated without nanoparticles was 0.89%. The apoptotic proportion was higher for the cube-like nano-CeO₂ than the other types. There were significantly greater rates of apoptosis in the nano-CeO₂-treated groups than in the untreated controls ($p < 0.01$).

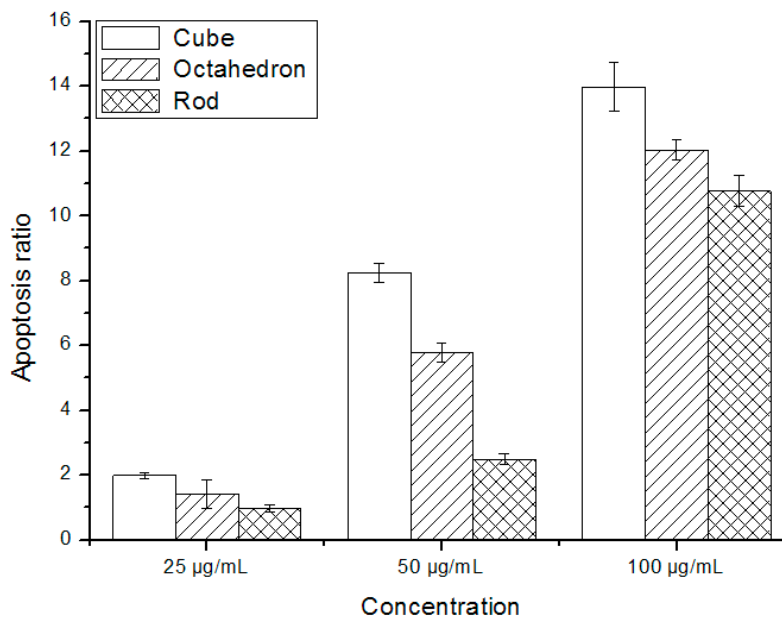


Figure 5. Percentage apoptosis of HepG2 cells after exposure to varying concentrations and types of nano-CeO₂ for 24 h.

3.4. The Cell Count, and MMP, ROS and GSH Levels Induced by Nano-CeO₂ in HepG2 Cells

High-content screening (HCS) is a novel method based on automated epifluorescence microscopy and acquired image analysis [21]. HCS has attracted attention as it can simultaneously measure multiple biomarkers in a single cell by multiplexed fluorescence measurements [22,23]. Application of HCS to organ-specific cell models provides deeper biological information suitable for better understanding the toxicity of compounds.

Figure 6A–C shows concurrent observations of cell count, and MMP, intracellular ROS and GSH levels that were observed in the HepG2 cells after each treatment. The HepG2 cells were monitored as cellular aggregates because real-time monitoring is required for live HepG2 cells. The average cellular hepatotoxic response of the HepG2 aggregates was obtained from the selection of cellular regions and the average value of the fluorescence cellular images in Figure 6A–C. The fluorescence intensity in the y-axis of Figure 6D–G corresponds to the average fluorescence intensity of the observed HepG2 cells acquired through the cellular region selection of three different cell culture plates. The cellular fluorescence intensities obtained from three different cell culture plates were averaged and this was plotted as a function of the dose.

After the treatment of HepG2 cells with the three different types of nano-CeO₂ at various concentrations, the fluorescence images of the HepG2 cellular aggregates are shown in Figure 6A–C. Then, a selection of identical cellular regions was executed with respect to all the fluorescence images of HepG2 aggregates acquired as a function of dose and their averaged fluorescence intensities were obtained. This process was applied to three different cell culture plates and the averaged value of the cellular fluorescence intensities obtained from individual cell culture plates was plotted as a function of dose as shown in Figure 6D–G. The fluorescence intensities in the y-axes of Figure 6D–G were normalized.

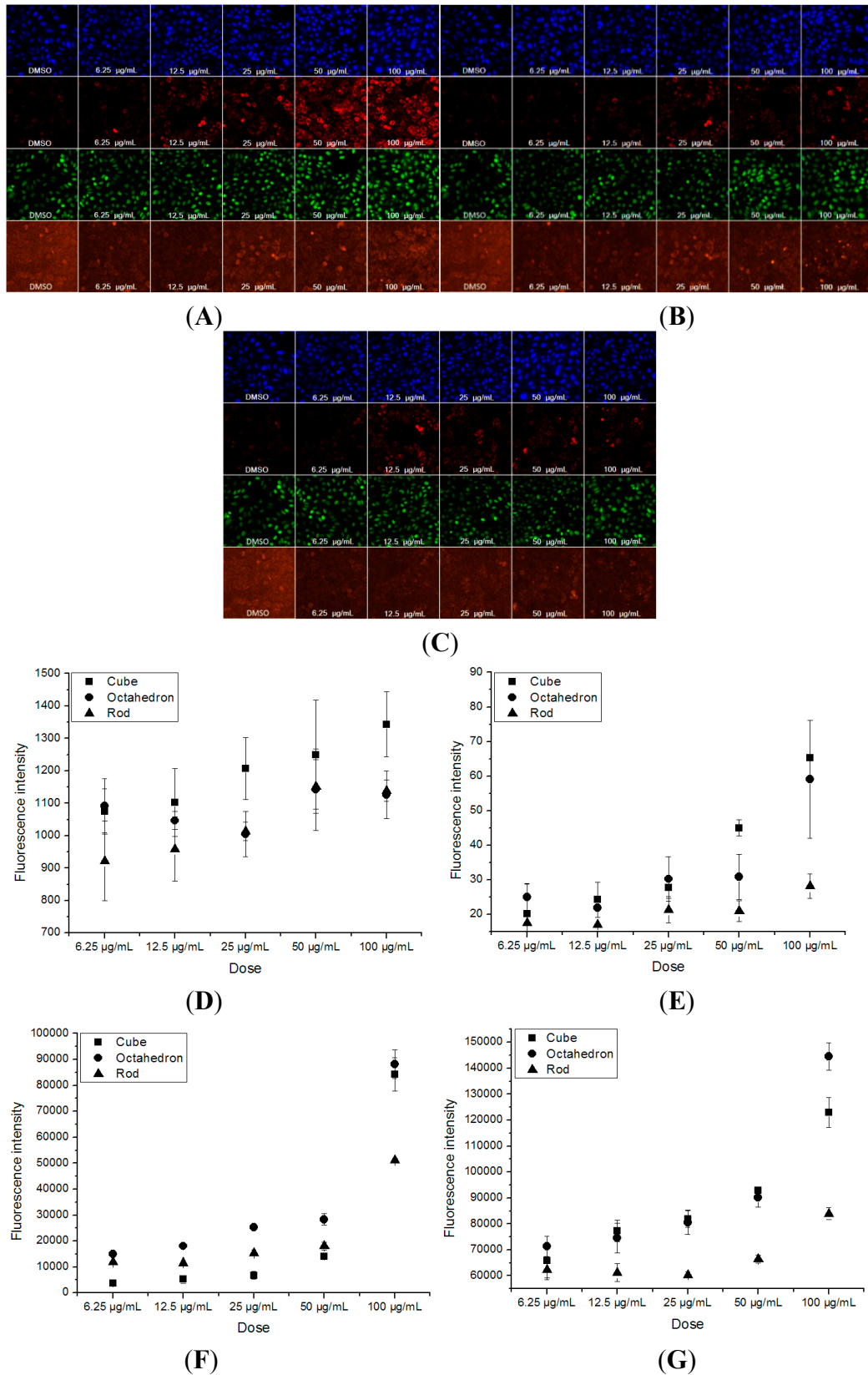


Figure 6. High-content screening of nano-CeO₂ induced hepatotoxicity. HepG2 cells were treated with cube- (A), octahedron- (B), and rod-like (C) nano-CeO₂ at various concentrations. The figures from top to bottom correspond to cellular images of cells count, MMP, ROS and GSH. Their normalized cellular fluorescence intensities were plotted as a function of treatment dose in cells count (D), MMP (E), ROS (F) and GSH (G).

As shown in Figure 6A–C, the fluorescence intensities for cell count, MMP, ROS, and GSH present different amounts of changes, which vary with increasing concentration of nano-CeO₂, for each morphology. These changes have certain dose-effect relationships, and are most sensitive in the cube-like groups. Hoechst 33342 allows the identification of individual cell nuclei, which permits a cell count by the nuclear area and allows subsequent analysis of the complementary staining to be conducted. A decrease in cell number indicates cell death and/or decreased cell proliferation. Nuclear shrinkage is typically a consequence of chromatin condensation and a sign of apoptotic cell death [24,25]. Additionally, the fluorescence intensity of Hoechst 33342 reflects the degree of apoptosis, because the apoptotic cells intake this dye more easily than living cells. Compared with the control (DMSO), the fluorescence intensity is distributed evenly and has no significant change in each group, except that the 100 µg/mL cube-like crystals induced a slight increase (Figure 6D). These results indicate that the cells did not undergo a lot of apoptosis or necrosis after each treatment.

Mitochondria are essential for the function and survival of cells. They are responsible for the generation of ATP, Ca²⁺ uptake and storage, and the generation and detoxification of reactive oxygen species [24]. Mitochondrial membrane potential changes has previously been identified as a sensitive predictor of human drug-induced liver injury [26,27]. TMRE was used to measure mitochondrial function, as it accumulates in mitochondria that have maintained their inner membrane potential. As shown in Figure 6E, the fluorescence intensity of MMP increased in the HepG2 cells treated with the cube-like nano-CeO₂ (the 100 µg/mL group was 2.8 times control). The rise in the MMP fluorescence intensity was gradual in the HepG2 cells treated with octahedron-like nano-CeO₂ (the 100 µg/mL group was only 1.4 times the control). However, the rod-like nano-CeO₂ showed a nearly constant MMP fluorescence intensity. The increase in TMRE brightness indicates mitochondrial hyperpolarization or a mitochondrial structural change that results in increased mitochondrial retention and/or fluorescence of TMRE [25]. Therefore, the most serious damage to the mitochondria was induced by the cube-like nano-CeO₂ and the most minimal by the rod-like nano-CeO₂. Due to the nanoparticles with various sizes and chemical compositions may attack mitochondria, which are redox-active organelles [12]. Nanoparticles may alter the production of ROS and interfere with antioxidant defenses, which will tend to induce oxidative stress [28–32]. To determine if nano-CeO₂ induces oxidative stress in human hepatoma HepG2 cells, we measured the ROS and antioxidase (GSH) production. Accumulation of fluorescent compound 2',7'-dichlorofluorescein (DCF), generated by intracellular oxidation of DHCF-DA, was used as an indicator of ROS generation, primarily H₂O₂. The production of ROS and MDA were found to increase after each treatment (Figure 6F,G). The maximum value of ROS was induced by 100 µg/mL of the cube-like nano-CeO₂, which was about 143% of the control. The ROS for the octahedron-like nano-CeO₂ was 120% of the control at 100 µg/mL. This level of ROS induced by the rod-like nano-CeO₂ was similar to the control at the same concentration. (Figure 6F). In the cube-like group, the GSH value increased with dose from 106% to 207% of the control. At the highest concentration (C_{max}), the octahedron-like group has a GSH value of 151% of control at maximum concentration, while the rod-like group reached only 130% at C_{max} (Figure 6G).

Based on these results, the cube-like nano-CeO₂ had an obvious effect on all four parameters. The octahedron-like had an effect on cell count, GSH and MMP, while the rod-like only increased GSH slightly. In summary, the toxicity of cube-like nano-CeO₂ was the highest, the octahedron-like was lower, and the rod-like was the lowest.

3.5. Antioxidant Activity of Nano-CeO₂

SWV has become one of the most sensitive methods for detecting DNA damage and antioxidant activity [20]. If nano-CeO₂ can protect DNA from damage by eliminating hydroxyl radicals ($\cdot\text{OH}$), the exposure of further guanine bases in DNA will be inhibited and the peak current of ruthenium (II) tris (2,2'-bipyridyl) ($[\text{Ru}(\text{bpy})_3]^{2+}$) will not be increased [20].

Our results (Figure 7) show the catalytic current of $[\text{Ru}(\text{bpy})_3]^{2+}$ for an oxidation peak at around +1.10 V that is due to the electrocatalytic oxidation of $[\text{Ru}(\text{bpy})_3]^{2+}$ by guanine bases in DNA. There is a major band for the intact double-stranded-DNA (lane A). When DNA was incubated in the solution of H₂O₂/Tris-HCl (pH 7.4), a new band (line E) could be seen that is due to DNA of different lengths, indicating that the DNA strands have been cut by $\cdot\text{OH}$. When each type of nano-CeO₂ (50 nM) was added to the system, the catalytic SWV current became smaller. The bands B and C came between lanes A and E, indicating the rod-like and octahedron-like nano-CeO₂, respectively, protected and inhibited DNA damage by scavenging ($\cdot\text{OH}$). Compared with bands B and C, band D nearly agrees with band E. This means that cube-like nano-CeO₂ did not eliminate $\cdot\text{OH}$.

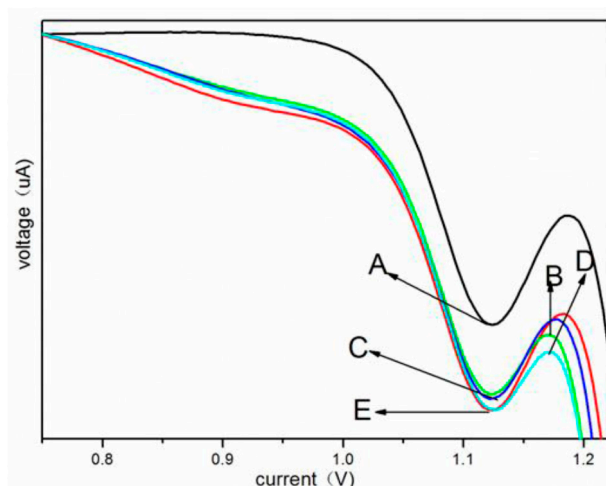


Figure 7. SWV scans in pH 7.0 PBS containing $[\text{Ru}(\text{bpy})_3]^{2+}$ (50 μM) for PDDA/DNA films incubated for 20min: (A) without other agents, (B) with rod-like nano-CeO₂, (C) with octahedron-like nano-CeO₂, (D) with cube-like nano-CeO₂, (E) with H₂O₂.

Repeatable redox cycles between Ce^{4+} and Ce^{3+} occur on the surface of nano-CeO₂ because of oxygen vacancies. The antioxidant activity of nano-CeO₂ originates from its remarkable redox properties, which can be determined by the rate of the redox cycle [24]. The oxidation-reduction properties for the nano-CeO₂ samples were determined by CO-TPR. The reduction peaks are shown in Figure 8. The low-temperature peak (<300 °C) was more important, for it is related to the reduction of surface oxygens. The results showed that the reduction peak of rod-like nano-CeO₂ first appears at around 100 °C and the total area was the largest, indicating it had the largest amount of surface oxygen and was the easiest to reduce. In contrast, the first reduction peak of the cube-like nano-CeO₂ was not detected until 300 °C with a very small peak. That is, the amount of surface oxygen was the least and it was the hardest to reduce. The octahedron-like was slightly easier to reduce than the rod-like but much harder than cube-like.

While the rate of nano-CeO₂ oxidation was fast, the reduction of ceria was generally sluggish [33]. Thus, the redox properties and the antioxidant ability of nano-CeO₂ were determined by its reducibility. In these results, the redox properties of the rod-like nano-CeO₂ was the best, which meant that rod-like nano-CeO₂ was the best at eliminating ROS. The cube-like was the worst with the octahedral somewhere in between. It is well known that the ability of nano-CeO₂ to eliminate ROS is related to its redox chemistry [28]. Perhaps, the cytotoxicity of the rod-like was the lowest because it was the most able to eliminate ROS, and cube-like was the highest because it was least able. From these results, we speculate that the redox properties of nano-CeO₂ may be an important factor in its cytotoxicity.

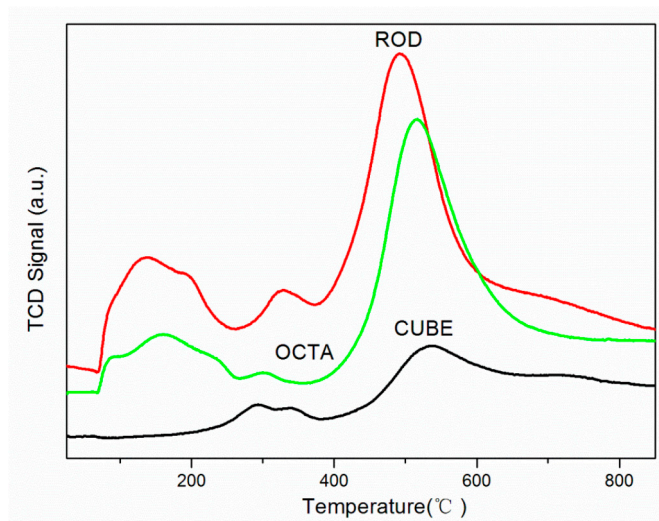


Figure 8. CO-TPR profiles of nano-CeO₂.

4. Conclusions

In summary, the *in vivo* cellular responses of HepG2 cells were measured following treatment with three types of nano-CeO₂ with different morphologies. Different concentrations of nano-CeO₂ had different toxicities on the HepG2 cells. The higher the concentration, the stronger the toxicity. At the same concentration, the nano-CeO₂ that had a smaller surface area produced higher cytotoxicity and lower antioxidative property. Therefore, rod-like nano-CeO₂ is a safer and more effective antioxidant when compared with octahedron and cube-like nano-CeO₂.

Acknowledgments

This work was supported by grants from Chinese Academy of Inspection and Quarantine (No. 2014JK009).

Author Contributions

Huiming Chen and Kebin Zhou had the original idea for the study and, with all co-authors carried out the design. Wenchao Ai and Lili Wang were responsible for recruitment and follow-up of study participants. Lili Wang, Wenchao Ai, Yanwu Zhai and Haishan Li prepared and applied the study.

Lili Wang was responsible for data cleaning and carried out the analyses. Wenchao Ai drafted the manuscript, which was revised by all authors. All authors read and approved the final manuscript.

Conflicts of Interest

The authors declare no conflict of interest.

References

1. Feng, X.; Sayle, D.C.; Wang, Z.L.; Paras, M.S.; Santora, B.; Sutorik, A.C.; Sayle, T.X.; Yang, Y.; Ding, Y.; Wang, X.; Her, Y.S. Converting ceria polyhedral nanoparticles into single-crystal nanospheres. *Science* **2006**, *312*, 1504–1508.
2. Guo, Z.; Du, F.; Li, G.; Cui, Z. Synthesis and characterization of single-crystal Ce(OH)CO₃ and CeO₂ triangular microplates. *Inorg. Chem.* **2006**, *45*, 4167–4169.
3. Yousef, J.M.; Mohamed, A.M. Prophylactic role of B vitamins against bulk and zinc oxide nano-particles toxicity induced oxidative DNA damage and apoptosis in rat livers. *J. Pharm. Sci.* **2015**, *28*, 175–184.
4. Frohlich, E.; Roblegg, E. Models for oral uptake of nanoparticles in consumer products. *Toxicology* **2012**, *291*, 10–17.
5. Ismael, R.P.; Soledad, G.; Javier, S.M.; Francisco, L.; Eloy, G.C.; Roberto, R.; Francisca, F.P. An insight into the mechanisms of Nano-CeO₂ toxicity in aquatic photosynthetic organisms. *Aquat. Toxicol.* **2012**, *122–123*, 133–143.
6. Zhang H, He X, Zhang Z, Zhang P, Li Y, Ma Y, Kuang Y, Zhao Y, Chai Z. Nano-CeO₂ exhibits adverse effects at environmental relevant concentrations. *Environ. Sci. Technol.* **2011**, *45*, 3725–3730.
7. Cheng, G.; Guo, W.; Han, L.; Chen, E.; Kong, L.; Wang, L.; Ai, W.; Song, N.; Li, H.; Chen, H. Cerium oxide nanoparticles induce cytotoxicity in human hepatoma SMMC-7721 cells via oxidative stress and the activation of MAPK signaling pathways. *Toxicol. In Vitro* **2013**, *27*, 1082–1088.
8. Kim, I.S.; Baek, M.; Choi, S.J. Comparative cytotoxicity of Al₂O₃, CeO₂, TiO₂ and ZnO nanoparticles to human lung cells. *J. Nanosci. Nanotechnol.* **2010**, *10*, 3453–3458.
9. Srinivas, A.; Rao, P.J.; Selvam, G.; Murthy, P.B.; Reddy, P.N. Acute inhalation toxicity of cerium oxide nanoparticles in rats. *Toxicol. Lett.* **2011**, *205*, 105–115.
10. Pagliari, F.; Mandoli, C.; Forte, G.; Magnani, E.; Pagliari, S.; Nardone, G; Licoccia, S.; Minieri M.; di Nardo, P.; Traversa, E. Cerium oxide nanoparticles protect cardiac progenitor cells from oxidative stress. *ACS Nano.* **2012**, *6*, 3767–3775.
11. Schubert, D.; Dargusch, R.; Raitano, J.; Chan, S.W. Cerium and yttrium oxide nanoparticles are neuroprotective. *Biochem. Biophys. Res. Commun.* **2006**, *342*, 86–91.
12. Xia, T.; Kovoichich, M.; Liang, M.; Mädler, L.; Gilbert, B.; Shi, H.; Yeh, J.I.; Zink, J.I.; Nel, A.E. Comparison of the mechanism of toxicity of zinc oxide and cerium oxide nanoparticles based on dissolution and oxidative stress properties. *ACS Nano.* **2008**, *2*, 2121–2134.

13. Chigurupati, S.; Mughal, M.R.; Okun, E.; Das, S.; Kumar, A.; McCaffery, M.; Seal, S.; Mattson, M.P. Effects of cerium oxide nanoparticles on the growth of keratinocytes, fibroblasts and vascular endothelial cells in cutaneous wound healing. *Biomaterials*. **2013**, *34*, 2194–2201.
14. Yang, Z.; Zhou, K.; Liu, X.; Tian, Q.; Lu, D.; Yang, S. Single-crystalline ceria nanocubes: Size-controlled synthesis, characterization and redox property. *Nanotechnology* **2007**, *18*, 1–4.
15. Zhou, K.; Li, Y. Catalysis based on nanocrystals with well-defined facets. *Angew. Chem. Int. Ed.* **2012**, *51*, 602–613.
16. Xu, Z.; Liu, C.; Wei, J.; Sun, J. Effects of four types of hydroxyapatite nanoparticles with different nanocrystal morphologies and sizes on apoptosis in rat osteoblasts. *J. Appl. Toxicol.* **2012**, *32*, 429–435.
17. Sahu, S.C.; Zheng, J.; Yourick, J.J.; Sprando, R.L.; Gao, X. Toxicogenomic responses of human liver HepG2 cells to silver nanoparticles. *J. Appl. Toxicol.* **2015**, *35*, 1160–1168.
18. Zhou, K.; Wang, X.; Sun, X.; Peng, Q.; Li, Y. Enhanced catalytic activity of ceria nanorods from well-defined reactive crystal planes. *J. Catal.* **2005**, *229*, 206–212.
19. Ahn, K.; Chung, Y.C.; Oh, J.H.; Prasad, D.H.; Kim, H.; Kim, H.R.; Son, J.W.; Lee, H.W.; Lee, J.H. A comparative study of catalytic partial oxidation of methane over CeO₂ supported metallic catalysts. *J. Nanosci. Nanotechnol.* **2011**, *11*, 6414–6419.
20. Xue, Y.; Zhai, Y.; Zhou, K.; Wang, L.; Tan, H.; Luan, Q.; Yao, X. The vital role of buffer anions in the antioxidant activity of CeO₂ nanoparticles. *Chemistry*. **2012**, *18*, 11115–11122.
21. O'Brien, P.J.; Irwin, W.; Diaz, D.; Howard-Cofield, E.; Krejsa, C.M.; Slaughter, M.R.; Gao, B.; Kaludercic, N.; Angeline, A.; Bernardi, P.; Brain, P.; Hougham, C. High concordance of drug-induced human hepatotoxicity with in vitro cytotoxicity measured in a novel cell-based model using high content screening. *Arch. Toxicol.* **2006**, *80*, 580–604.
22. Wlodkovic, D.; Khoshmanesh, K.; Sharpe, J.C.; Darzynkiewicz, Z.; Cooper, J.M. Apoptosis goes on a chip: Advances in the microfluidic analysis of programmed cell death. *Anal. Chem.* **2011**, *83*, 6439–6446.
23. Michelini, E.; Cevenini, L.; Mezzanotte, L.; Ablamsky, D.; Southworth, T.; Branchini, B.; Roda, A. Spectral-resolved gene technology for multiplexed bioluminescence and high-content screening. *Anal. Chem.* **2008**, *80*, 260–267.
24. Ramery, E.; O'Brien, P.J. Evaluation of the cytotoxicity of organic dust components on THP1 monocytes-derived macrophages using high content analysis. *Environ. Toxicol.* **2014**, *29*, 310–319.
25. Abraham, V.C.; Towne, D.L.; Waring, J.F.; Warrior, U.; Burns, D.J. Application of a high-content multiparameter cytotoxicity assay to prioritize compounds based on toxicity potential in humans. *J. Biomol. Screen.* **2008**, *13*, 527–537.
26. Donato, M.T.; Tolosa, L.; Jiménez, N.; Castell, J.V.; Gómez-Lechón, M.J. High-content imaging technology for the evaluation of drug-induced steatosis using a multiparametric cell-based assay. *J. Biomol. Screen.* **2012**, *17*, 394–400.
27. Tolosa, L.; Pinto, S.; Donato, M.T.; Lahoz, A.; Castell, J.V.; O'Connor, J.E.; Gómez-Lechón, M.J. Development of a multiparametric cell-based protocol to screen and classify the hepatotoxicity potential of drugs. *Toxicol. Sci.* **2012**, *127*, 187–198.

28. Srinivas, A.; Rao, P.J.; Selvam, G.; Goparaju, A.; Murthy, P.B.; Reddy, P.N. Oxidative stress and inflammatory responses of rat following acute inhalation exposure to iron oxide nanoparticles. *Hum. Exp. Toxicol.* **2012**, *31*, 1113–1131.
29. Saquib, Q.; Al-Khedhairi, A.A.; Siddiqui, M.A.; Abou-Tarboush, F.M.; Azam, A.; Musarrat, J. Titanium dioxide nanoparticles induced cytotoxicity, oxidative stress and DNA damage in human amnion epithelial (WISH) cells. *Toxicol. In Vitro.* **2012**, *26*, 351–361.
30. Sayes, C.M.; Gobin, A.M.; Ausman, K.D.; Mendez, J.; West, J.L.; Colvin, V.L. Nano-C60 cytotoxicity is due to lipid peroxidation. *Biomaterials* **2005**, *26*, 7587–7595.
31. Adams, L.K.; Lyon, D.Y.; McIntosh, A.; Alvarez, P.J. Comparative toxicity of nano-scale TiO₂, SiO₂ and ZnO water suspensions. *Water Sci. Technol.* **2006**, *54*, 327–334.
32. Zhang, H.; He, X.; Zhang, Z.; Zhang, P.; Li, Y.; Ma, Y.; Kuang, Y.; Zhao, Y.; Chai, Z. Nano-CeO₂ exhibits adverse effects at environmental relevant concentrations. *Environ. Sci. Technol.* **2011**, *45*, 3725–3730.
33. Liu, X. Zhou, K.; Wang, L.; Wang, B.; Li, Y. Oxygen vacancy clusters promoting reducibility and activity of ceria nanorods. *J. Amer. Chem. Soc.* **2009**, *131*, 3140–3141.

© 2015 by the authors; licensee MDPI, Basel, Switzerland. This article is an open access article distributed under the terms and conditions of the Creative Commons Attribution license (<http://creativecommons.org/licenses/by/4.0/>).